Research Paper

Exploring density and strength variations in asteroid 16 Psyche's composition with 3D hydrocode modeling of its deepest impact structure

Wendy K. Caldwell *, Abigail Hunter, Catherine S. Plesko

X-Computational Physics Division, Los Alamos National Laboratory, Los Alamos, NM 87545, United States of America

ARTICLE INFO

ABSTRACT

Asteroid 16 Psyche is the largest metallic Main Belt Asteroid and is the subject of a forthcoming NASA mission. The composition of Psyche is still unknown and subject of recent debate. In particular, how much porosity is within Psyche, along with how much of Psyche consists of non-metallic versus metallic materials, are central questions to the issue of Psyche's composition. If Psyche is indeed predominantly composed of metallic materials, it would need to have considerable porosity ($\sim$ 30%–50%) for a composition consistent with its expected bulk density ($\sim$ 3.7–4.1 g/cm^3). In this work, we vary the density and strength of Psyche by including uniform and layered fields of pseudo-microporosity, in addition to investigating the presence of macroscopic voids, i.e., spaces larger than the size of the simulation's mesh cells, in rubble-pile configurations. All configurations result in bulk densities within the uncertainties of measured values, however the strength of Psyche and the distribution of pseudo-pores are varied. Through 3D computational models of Psyche's deepest impact structure, we show that Psyche's composition is unlikely to contain only pseudo-microporosity. Rather, rubble pile structures, which include macroscopic voids, are shown to match the crater's measured aspect ratio better than simulations of structures that included only pseudo-microporosity.

1. Introduction

Asteroid (16) Psyche (henceforth referred to as Psyche), the largest M-type (metallic) Main Belt Asteroid (MBA), is the subject of a forthcoming National Aeronautics and Space Administration (NASA) discovery mission (Lupishko, 2006; Oh et al., 2016). The mission will be the first of its kind to explore a metallic asteroid (Oh et al., 2016). In response to this mission, there have been many recent efforts using experimental, observational, and modeling techniques to investigate Psyche. Of the many aspects that can be investigated, one of the fundamental remaining questions about Psyche is its composition. Earth-based measurement techniques estimate that Psyche has a bulk density range of 1.1–7.6 g/cm^3, though the majority of these estimates have ranges of 3.7–4.1 g/cm^3 (Lupishko, 2006; Viateau, 2000; Kochetova, 2003; Shepard et al., 2017; Elkins-Tanton et al., 2020; Siltala and Granvik, 2021). Recent estimates for bulk densities within the median range have called into question that Psyche is an intact metal (iron) core remnant. These bulk density estimates indicate that Psyche either has considerable porosity, considerable non-metallic constituents, or a combination of both. The degree of porosity and amount of non-metallic materials comprising Psyche is one of the most pressing questions regarding Psyche's composition (Elkins-Tanton et al., 2020).

In this work, we particularly focus on variation of density and strength within Psyche, which could be representative of some non-metallic component of the asteroid, which may be porosity or some other material. We consider what we term as 'pseudo-microporosity' and 'macroscopic voids' present within Psyche that results in configurations that are consistent with measured bulk density estimates. Pseudo-microporosity within the asteroid is meant to be representative of a structure that has been fractured through numerous hit-and-run collisions, resulting in a porous aggregate. In this case, small cracks and voids, which are comparable to the material's grain size, are distributed throughout the asteroid (Flynn et al., 1999). The primary difference between pseudo-microporosity as modeled here and more realistic cracks and voids is that modeling constraints the pseudo-microporosity model used in this study do not include PdV work done by pore compaction processes, which can affect shock attenuation, thermal response, ejecta speed, and other physics (Melosh, 1989, 2011). We highlight that the primary focus of this work is a comparison of the resulting crater profiles with those that have been measured. For this application, the pseudo-microporosity provides a way to vary Psyche's density, and corresponding strength, so that the impact on the crater shape can be investigated. The pseudo-microporosity also allows us to

---

* Corresponding author.
  E-mail address: wkcaldwell@lanl.gov (W.K. Caldwell).

vary the distribution of the pseudo-microporosity so uniform versus layered target configurations can be studied.

On a larger length scale, macroscopic voids or macroporosity is representative of a rubble-pile structure, in which case the asteroid was shattered by previous impacts and then re-accreted into a single body with macroscopic density variations (Flynn et al., 1999). Interestingly, Psyche's mass, estimated to be 0.54–1.8 $\times 10^{-11} M_\odot$ (solar mass) (Lupishko, 2006) is on the order of 10^{19} kg, near the threshold (i.e., $\geq 10^{20}$ kg) at which one might expect high interior pressures to compact or crush out much of the asteroid's macroporosity (Carry, 2012). However, this threshold value is based on the pressures needed for silicate grain compaction, and the higher strength of the metal constituents within Psyche may withstand higher internal pressures than Psyche reaches under hydrostatic equilibrium. Hence, it is reasonable to consider the possibility of several different types of porosity within Psyche's structure, such as uniform pseudo-microporosity, layered pseudo-microporosity (with lower pseudo-porosity values in the interior and a less dense regolith at the surface), and macroscopic voids or rubble-like structures, all of which could result in current bulk density estimates of Psyche. Ultimately, it is likely that Psyche includes porosity across a wide range of length scales.

Micro- and macro-porosity have been previously shown to have notable effects on the structure of craters in highly porous materials (e.g., silicates and chondrites) resulting from high-velocity impacts (Housen and Holsapple, 2003; Housen et al., 1999; Flynn et al., 1999). Thus, the morphology of craters on asteroids can provide information that can help to constrain Psyche's bulk properties. Psyche's Southern hemisphere has two such large impact structures (Shepard et al., 2017). Modeling the formation of either of these impact sites on Psyche can help to inform the current understanding of Psyche's composition. With relatively little cost, computational models provide the chance to explore many possible compositions of Psyche with the same or similar bulk densities; comparison of predicted crater structures to known measurements can help to eliminate unlikely compositions.

Typically, models operative at the largest of length scales are used to model impact craters in planetary science applications. Generally, hydrodynamic codes, or hydrocodes, are used because they can capture shock wave processes in various types of materials (i.e., gas, liquid, solid, and combinations thereof). For applications in planetary science, several studies have benchmarked hydrocodes using impact cratering simulations (Pierazzo et al., 2008; Caldwell et al., 2018; Stickle et al., 2020). These studies included both solution verification for physical quantities in both the strength-dominated and gravity-dominated regimes of impact crater formation and validation comparisons to experimental results of laboratory-scale, high-velocity impacts into fluid and solid targets. Recently, Raducan et al. (2020) used the iSALE code to investigate several possible internal asteroid structures that may explain Psyche's composition by modeling impact crater formation. More specifically, they investigated the effect of microporosity within possible iron-rock layer configurations. These simulations found that the crater structures varied from bowl-shaped structures when Psyche's near-surface structure was assumed to be homogeneous to shallower craters with flat floors when Psyche was assumed to have a layered structure. While this paper addresses important questions about microporosity along with the possible presence and structure of the non-metallic components within Psyche, it does not consider the effect of varying amounts of microporosity, the possibility of macroporosity, Psyche's curved surface, or oblique impacts on the crater morphology. This work aims to address some of these possibilities.

Previously, we modeled the formation of Psyche's largest impact structure using the arbitrary Lagrangian–Eulerian (ALE) hydrocode FLAG (Caldwell et al., 2020). This work primarily focused on investigating possible metallic materials that could comprise Psyche (namely, nickel, iron, and the Monel alloy), and the effect of uniform pseudo-microporosity. Simulations were completed in 3D, and best matches to measured crater dimensions were found using the Monel alloy

with about 30%–50% pseudo-microporosity. These results were in good agreement with calculations presented by Elkins-Tanton et al. (2020), which show that if non-metallic components are not considered, Psyche's porosity is expected to be 40%–50%. However, we note that Elkins-Tanton et al. assumed Psyche to be a kamacite body (ρ_{kam} = 7.870 g/cm^3), which has a slightly lower density than the Monel alloy (ρ_{mon} = 8.81 g/cm^3). If Monel is considered to be the primary metallic component comprising Psyche, the expected porosity will slightly increase to ~50%–60%. Thus, high porosity within Psyche remains a possibility, particularly if Psyche's composition is dominated by metallic materials.

Extending beyond our original study, this work seeks to further explore the effects of internal composition on crater formation by simulating Psyche's deepest impact structure (i.e., a different impact structure than that modeled in our previous work) (Caldwell et al., 2020), located in its Southern hemisphere, with an estimated depth of 6.4 ± 0.64 km and an estimated diameter of 53 ± 15 km (Shepard et al., 2017). In particular, we consider varying amounts of uniform and layered pseudo-microporosity, along with rubble-pile configurations, which include both macroscopic voids and pseudo-microporosity. By varying the density and strength of Psyche, we test a number of potential compositions with bulk densities within the range of estimates obtained from other measuring techniques.

The methods and results of this paper are organized as follows: Section 2 describes details of the different models used in this study, including the material models and a brief summary of the FLAG hydrocode; Section 3 presents preliminary results in preparation for our density composition study, including variations in impactor mass and momentum; Sections 4–6 then present results for uniform pseudo-microporosity, layered pseudo-microporosity structures, and rubble piles, respectively. In all cases, a set of 2D simulations are completed first, followed by 3D simulations of compositions shown to produce promising crater dimensions in the 2D scoping studies. Section 7 presents discussion of these results, followed by final conclusions in Section 8.

2. Methodology

For all simulations completed as part of this work, we used the ALE hydrocode FLAG, developed and maintained by Los Alamos National Laboratory (Hill, 2017; Burton, 1992, 1994b,a). FLAG has been previously verified and validated for impact cratering problems (Caldwell et al., 2018, 2021) and has been used for planetary science applications (Caldwell et al., 2020; Plesko et al., 2019). FLAG is a multi-physics hydrocode with a variety of material modeling and equation of state (EOS) capabilities (Hill, 2017; Burton, 1992, 1994b,a). FLAG can be used for simulations in 1–3 spatial dimensions with Lagrangian, Eulerian, or ALE strategies, including adaptive mesh refinement (AMR) (Hill, 2017; Burton, 1992, 1994b,a; Kenamond, 2020).

Because our simulations focused primarily on density composition rather than material, we chose to use the alloy Monel for both target and impactor in all simulations. For completeness, Section 3 shows 2D impact crater results for varying impactor and target materials for solid materials. As discussed previously, pseudo-porous Monel was used in our prior study of Psyche and produced crater dimensions within the uncertainties of the measured dimensions (Caldwell et al., 2020). Monel is a nickel alloy with a solid density of 8.81 g/cm^3 and is likely extraterrestrial in origin, which makes it a reasonable choice for modeling metallic asteroids (Shoemaker and Smith, 2006; Riller, 2005). Monel also contains small amounts of non-metallic materials that are common in solid bodies in the solar system. Thus, we use Monel for both the target and impactor material, and vary the amount and type of pseudo-porosity in Psyche to gain further insight into Psyche's probable composition given current bulk density estimates.

For the EOS, we used an analytic Mie–Grüneisen EOS, which is an appropriate choice for these simulations because melt is not expected

to play a significant role (Melosh, 2011). Previous work modeling impacts in FLAG explored EOS choice and found only miniscule differences between physical properties when only the EOS varied (Caldwell et al., 2018; Caldwell, 2019). We used the Steinberg–Guinan constitutive model (Steinberg et al., 1980) to model the material flow stress and shear modulus, which have dependence on the material density, pressure, and temperature. In addition, when pseudo-microporosity is considered, the material flow stress and shear modulus are first calculated using the solid material density and then adjusted using a volume-fraction weighting based on the total void volume within a computational zone. The flow stress and shear modulus are updated at every time step. Damaged material was defined by minimum pressure and compression values. The Steinberg–Guinan model was designed to model flow stress behavior in metals at high strain rates (up to $\sim 10^5$ s^{-1}) (Steinberg et al., 1980). Since its development, the model has been tested over a wide variety of high-rate loading conditions, including impact loading conditions, and presented reasonable comparison to experimental data (Caldwell, 2019; Peng et al., 2008; Krygier et al., 2019; Vogler et al., 2009; Harrison et al., 1995). The model parameters for Monel for both the Mie–Grüneisen EOS and the Steinberg–Guinan strength model were taken from Steinberg (1996). No additional efforts were made to optimize the parameter set. Relevant parameters for these models are included in Appendix B. To account for the effect of pseudo-microporosity within Psyche on the volumetric response, the pressure is first determined at each time step using the Mie–Grüneisen EOS and the solid material density. Quantities calculated with the EOS, including the pressure and bulk modulus, are then adjusted to account for pseudo-microporosity using a volume-fraction weighting based on the total void volume within a computational zone, which is consistent with adjustments made to the flow stress and shear modulus to account for pseudo-microporosity. A separate compaction model was not used in this approach, and previous work using FLAG to model impacts into pseudo-porous materials matched measured crater dimensions within the uncertainties and compared well to other computational models of porous-target impacts (Kumamoto et al., 2022; Stickle et al., 2022; Caldwell et al., 2020). A failure criteria was also employed such that regions with a specified minimum pressure or compression would fail, meaning these computational cells no longer maintained any material strength. This choice was made to capture the effect of tensile regions created by shock wave interaction that may cause spallation. The material surrounding Psyche, including the space between boulders in the rubble piles, was modeled as void.

All calculated (2D and 3D) crater profiles were compared to crater dimensions from radar shape model data (Shepard et al., 2017) and to the theoretical pre-modification crater (henceforth denoted the transient crater) (Melosh, 2011). The transient crater was calculated assuming a normal impact into a metallic target using Holsapple's transient crater formulas (Holsapple, 1993). Because the resulting crater was spherical, we defined the transient crater as the portion of the sphere cut by a plane that produced the correct depth predicted by the Holsapple calculations. Note that the spherical transient crater is defined as the maximum diameter and depth the cavity attains before the crater modification stage begins (Melosh, 1989; Holsapple, 1993). The radar shape model data provided a picture of the crater's shape after extensive time had passed, and the crater's morphology has since likely evolved as a result of strength and gravity effects along with processes such as impact gardening and erosion. Our current modeling approach did not account for all of these effects, as the long time scales on which these processes occur are not conducive to computational modeling in hydrocodes. Thus, the current crater dimensions determined from the radar shape model data are likely shallower than those following the formation of the crater. The transient crater dimensions offered an alternate perspective to the radar shape model. Namely, the transient crater provided dimensions prior to crater collapse, i.e., before any material settled down into the newly formed crater (Grieve, 1991; Melosh,

1989; Grieve and Cintala, 1982; French, 1998). Thus, the transient crater dimensions were expected to be deeper than estimated crater dimensions from observational data. We note that the transient crater calculation presented in this work is based on a normal impact and will likely be larger (deeper and wider) than a transient crater formed via an oblique impact. Overall, promising calculated crater dimensions in 2D, in which only normal impacts can be modeled, were identified as those between (or very close to) the transient crater dimensions and those taken from the radar data. Specifically, reasonable crater dimensions would have depths near that of the transient crater profile. Simulations that resulted in promising crater dimensions in 2D were then tested in 3D, in which oblique impacts could be considered.

It is highly likely that the craters on Psyche were formed via oblique impacts (Caldwell et al., 2020; Melosh, 2011; Lupishko, 2006). The crater shape can vary with the impact angle, and capturing this aspect in 3D can be important for accurate comparisons to available data. Generally, oblique impact angles produce shallower craters, and the amount of excavated mass decreases with increasing obliquity (Gault and Wedekind, 1978; Suzuki et al., 2021; Elbeshausen and Wunnemann, 2013; Nishida et al., 2019). While the crater depth can show notable differences with relatively small changes in impact angle, the crater diameter (length and width) changes at a slower rate with elongated shapes achieved at highly oblique impact angles (Melosh, 2011; Burchell and Whitehorn, 2003; Ogawa et al., 2021; Burchell and Mackay, 1998; Davison et al., 2011). For 3D rubble piles, impacts will also be compared based upon the location at which the impactor strikes the boulder(s). All systems are first tested in 2D, and if the crater profile is promising (meaning a crater depth near to that of the transient crater and narrower crater diameter), then the system is selected for 3D simulations. For rubble pile simulations, oblique impact angles are explored to determine the effects of impact location when the angle of impact results in a change in the impact surface (e.g., a direct impact on a single boulder versus an impact that strikes several boulders at an angle). Additional rubble-pile simulations compared varying impact angles striking the same location on Psyche to allow for a more direct comparison of the effects of impact angle on crater morphology.

In the cases of uniform pseudo-microporosity and pseudo-microporosity within layered structures, unless otherwise indicated, the Monel impactor initial conditions were a sphere (3D) or semicircle (2D) of radius 3.75 km, with a mass of 1.94e15 kg and an impact velocity of 4.5 km/s (Farinella and Davis, 1992). The Monel target was modeled using a shape model (Shepard et al., 2017) with a spherical cap of radius 110 km (3D) to cover pre-existing craters in the impact area (see Figs. 1(a)–1(c)) or a semicircle (2D) of radius 125 km (Caldwell, 2019; Caldwell et al., 2020). For simulations in which impactor size and velocity were varied, mass and velocity are discussed in the relevant sections. In the layered structures, Psyche was modeled with a denser core region surrounded by a less dense mantle region, and the radius of the core region varied across simulations with the total target radius remaining 125 km. The 2D simulations for uniform and layered pseudo-microporosity used axisymmetric boundary conditions, and the initial simulation geometries are shown in Figs. 2(a)–2(d). We note that with axisymmetric boundary conditions, the 2D semicircular impactor and target are revolved about the midline and thus simulate spherical regions. The rubble piles were modeled with both a regular hexagonal close packing and a regular square packing. Each packing consisted of spheres (3D) or circles (2D) with radii of 12.5 km. The maximum target radius and impactor size and velocity were the same as those used for the uniform/layered pseudo-microporosity simulations. These simulations were in a Cartesian coordinate system in order to avoid extraneous hoop stresses that would be present in an axisymmetric simulation of this arrangement. Because the 2D rubble-pile simulations used Cartesian coordinates, the circles comprising the impactor and target rubble pile represent infinitely long cylinders. This modeling choice ensures that the rubble piles are not simulated as stacked tori,
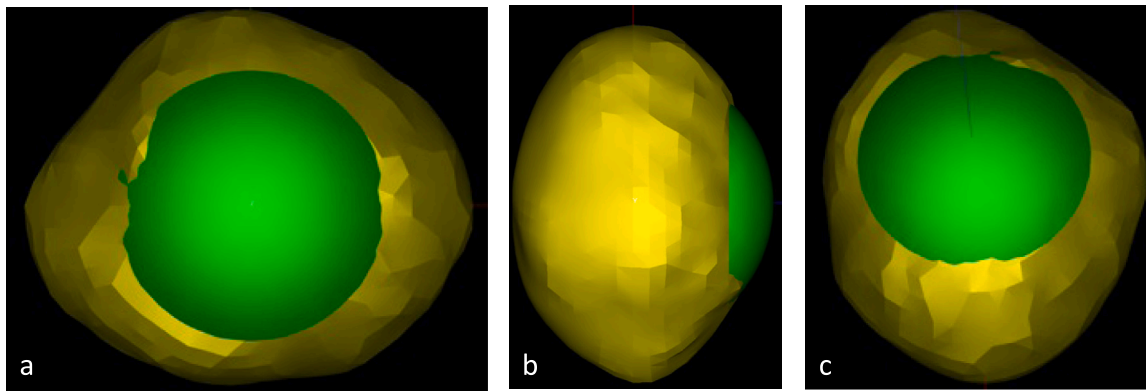
Fig. 1. Psyche shape model (yellow) and spherical cap (green), showing the 3D Psyche model used in this study. The spherical cap was added to cover the existing craters, which were re-created numerically in this study Figure (a) shows the overhead view of the spherical cap, (b) shows a side view, and (c) presents an angled view of the spherical cap. (For interpretation of the references to color in this figure legend, the reader is referred to the web version of this article.)

which would introduce artificial hoop stresses if run on a 2D axisymmetric mesh. Figs. 2(e)–2(f) show the 2D rubble-pile simulations at initialization, and Figs. 3(a)–3(c) show the 3D rubble-pile simulations at initialization.

Simulations ran to a maximum time of 381 s, which allows for sufficient time for the crater modification stage with a substantial buffer period to account for uncertainties (Caldwell, 2019). Because of the significant run times of some simulations, they would be restarted several times until completed. In these instances, simulations were checked prior to restarting to determine whether target material was still moving out of the crater and if any material velocity exceeded escape velocity. If the material had settled, the simulation was not restarted, and crater measurements were taken. Thus, while simulations had different run times in some cases, each simulation was "complete" in the sense that the transient crater formation had completed, and the crater had entered the quasi-static modification stage. The simulation stopping time was calculated based on the relationship between crater formation time and volume of excavated material, which was based on observational and theoretical crater measurements. Our method used an adaptive time step and an Eulerian mesh relaxer. The 2D simulations used a mesh with a uniform zone size equivalent to about 11 cells per projectile radius (cppr), while the 3D simulations, unless otherwise indicated, used a varied mesh resolution of 5 cppr around the point of impact, coarsening farther from the region of interest. Fig. 2(a) shows the mesh resolution used in each of the 2D simulations, and Fig. 3(a) shows the mesh resolution for 3D simulations, including the computational mesh.

The 2D simulations ran on either 36 cores, with run times ranging from 8.8–21.3 h, or 180 cores, with run times ranging from 1.3–39.5 h. Solid-target simulations ran for shorter times (about 3–4 h), while more complicated simulations with porosity required greater computational resources. The 3D solid simulations ran on 1080 cores for 16.8–18.4 h, while 3D uniform pseudo-microporosity simulations ran on 1440 cores for about 50 h. The 3D rubble pile simulations ran on 2484 cores for 22.3–29.0 h.

3. Scoping study of materials and kinetic energies

While our primary focus is how Psyche's composition impacts crater shape, we first include a brief section in which we vary impactor and target properties for completeness. We note that these cases are meant to provide bounds for better constraining crater dimensions and, thus, we did not expect all of these simulations to result in craters within uncertainty measurements. In this section, we explore different materials for Psyche, different impactor sizes, and different impact velocities. While the broader scope of this work focuses primarily on composition, this section can help to frame those results in context

when considering other variables, such as impactor mass or impact momentum.

In our previous work, we found that kinetic energy (KE), the impactor mass multiplied by the square of the impact velocity, was a key variable (Caldwell et al., 2020). Impactors of less dense material with equivalent KE to their denser metallic counterparts resulted in similar crater dimensions. Before exploring varying internal compositions, we first consider impacts into solid models of Psyche. In these preliminary simulations, we modeled Psyche as solid Monel, solid nickel, and solid iron. We modeled the impactor as solid Monel, solid nickel, solid iron, and solid silicon dioxide (SiO_2). Because of the noteworthy difference in density, and thus, mass and KE between SiO_2 and metallic impactors, we considered SiO_2 impactors with equivalent radii to metallic impactors, denoted with subscript RAD, and SiO_2 impactors with equivalent KE to metallic impactors, denoted with subscript KE. Each of these solid simulations was run in 2D with axisymmetry, using an impact velocity of 4.5 km/s.

Fig. 4 shows the results of these preliminary solid simulations. In the figure's legend, impactor materials are listed first, and the target materials are listed second. Note the three smallest craters from these simulations resulted from SiO_2 impactors with equivalent radii of metallic impactors. Because of the lower densities of these impactors, the mass and KE were lower than for metallic impactors. As expected, in these cases, the craters were smaller. In contrast, when an impactor of SiO_2 had equivalent KE of a metallic impactor, the resulting crater was much larger than in the previous case and excavated a similar amount of material as a metallic impactor with the same KE. As expected, hypervelocity cratering properties depend strongly on the KE of the impact in this regime, in which material strength dominates crater formation. For much larger impacts, in which gravity is dominant, such relationships are not a given, and other factors determine features of the cratering process (Holsapple, 1993). The current work focuses only on the strength regime.

Because previous results have largely consisted of craters that were too large, we ran additional 2D simulations to explore impactor size (mass) and impact velocity (momentum) in both solid and 50% pseudo-porous targets. We considered three impactor diameters: 10 km, 12.5 km, and 15 km. The respective impactor masses were 4.61e15 kg, 9.00e15 kg, and 1.56e16 kg. The respective KEs of the impacts were 9.34e22 J, 1.82e23 J, and 3.16e23 J. Table 1 shows the crater dimensions from these simulations. As expected, impacts into pseudo-porous targets resulted in larger craters than impacts into solid craters when the impactor was the same. Likewise, larger impactors resulted in larger craters when the target was the same.

We also ran simulations varying impact velocity. We tested impact velocities of 4 km/s, 5.5 km/s, 6.5 km/s, 7 km/s, 8.5 km/s, 9 km/s, 10 km/s, and 12 km/s (Farinella and Davis, 1992). The impactor mass did
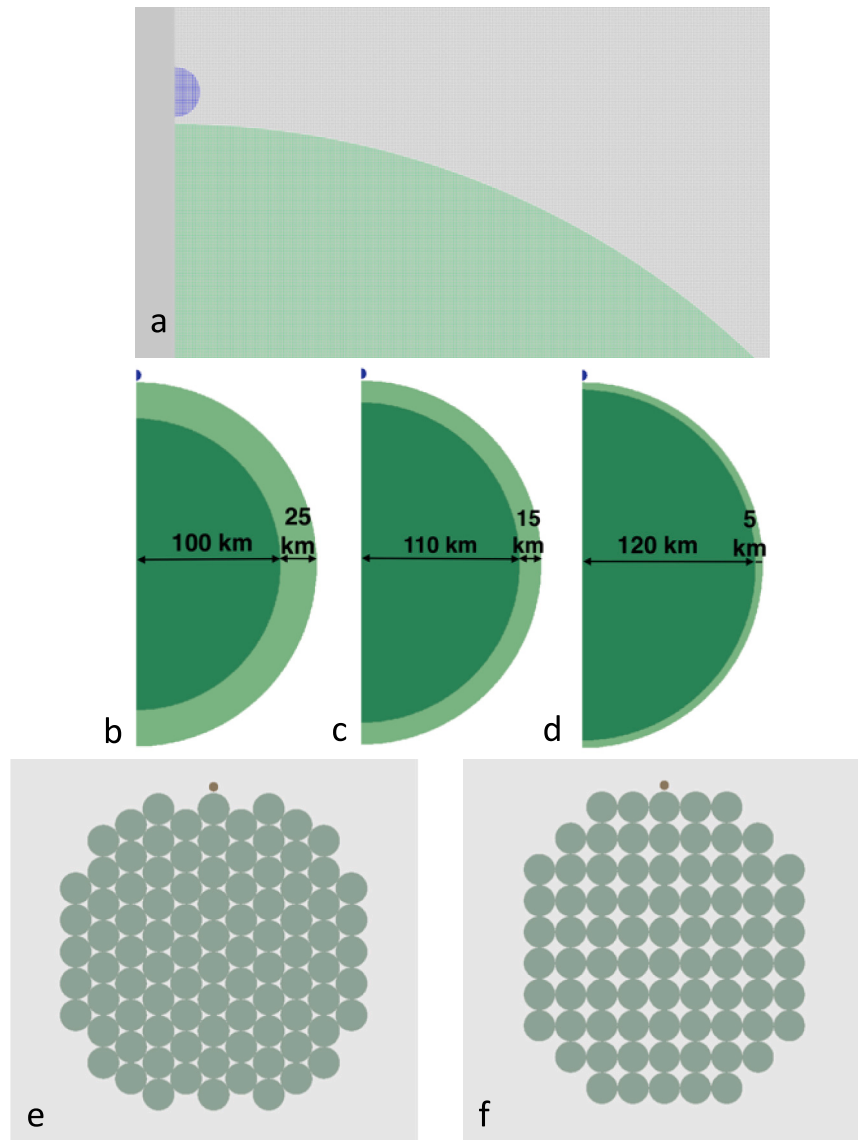
Fig. 2. 2D simulations at initialization, showing setups for (a) uniform pseudo-microporosity (zone size 330 m), (b)-(d) layered pseudo-microporosity, and (e)-(f) rubble-pile configurations. The 2D simulations utilize axisymmetric boundary conditions, and the layered pseudo-microporosity cases include 3 different core radii. In the rubble-pile configurations, the circles represent boulders of 25 km in diameter; they are not smooth-particle hydrodynamics (SPH) particles.

Table 1
Results from 2D axisymmetric simulations varying impactor diameter for both solid and 50% pseudo-porous targets.

Impactor diameter	Pseudo-Porosity	Crater radius (km)	Crater depth (km)
10 km	solid	14.75	14.57
10 km	50%	16.15	20.60
12.5 km	solid	18.95	20.54
12.5 km	50%	23.20	18.75
15 km	solid	23.10	25.32
15 km	50%	26.25	41.00

not change, as in the previous cases, but the KE changed as a result of the velocity change. The respective KE of these impactors was 3.10e22 J, 5.87e22 J, 8.20e22 J, 9.51e22 J, 1.40e23 J, 1.57e23 J, 1.94e23 J, and 2.79e23 J. Table 2 shows these results.

While these preliminary results add completeness to our study by exploring impactor mass and momentum through variations of material properties, impactor size, and impact velocity, the primary focus of this study is the effect of target density composition on crater formation.

Thus, in the remaining sections, a single impactor model is used for consistent size, shape, mass, and KE. This impactor had a diameter of 7.5 km, a velocity of 4.5 km/s, a mass of 1.94e15 kg, and a KE of 3.93e22 J. Keeping the physical properties of the impactor constant will provide more insight into the effects of density and corresponding strength variations within Psyche.

4. Uniform pseudo-microporosity results

To begin, we consider Psyche as an homogeneous body with pseudo-microporosity uniformly distributed throughout, resulting in a constant, but degraded, density throughout the asteroid. In 2D, we considered pseudo-microporosity values of 30%, 40%, and 50%, resulting in bulk density values of 6.167 g/cm^3, 5.286 g/cm^3, and 4.405 g/cm^3, respectively. Fig. 5 shows the crater profiles from these simulations, along with the crater profile from a simulation in which the target was assumed to be solid. Simulations with 40% and 50% pseudo-microporosity ran to the maximum time of 381 s. The simulation with 30% pseudo-microporosity ran to 162.1 s, at which point all ejected material had been expelled from the crater. As expected,
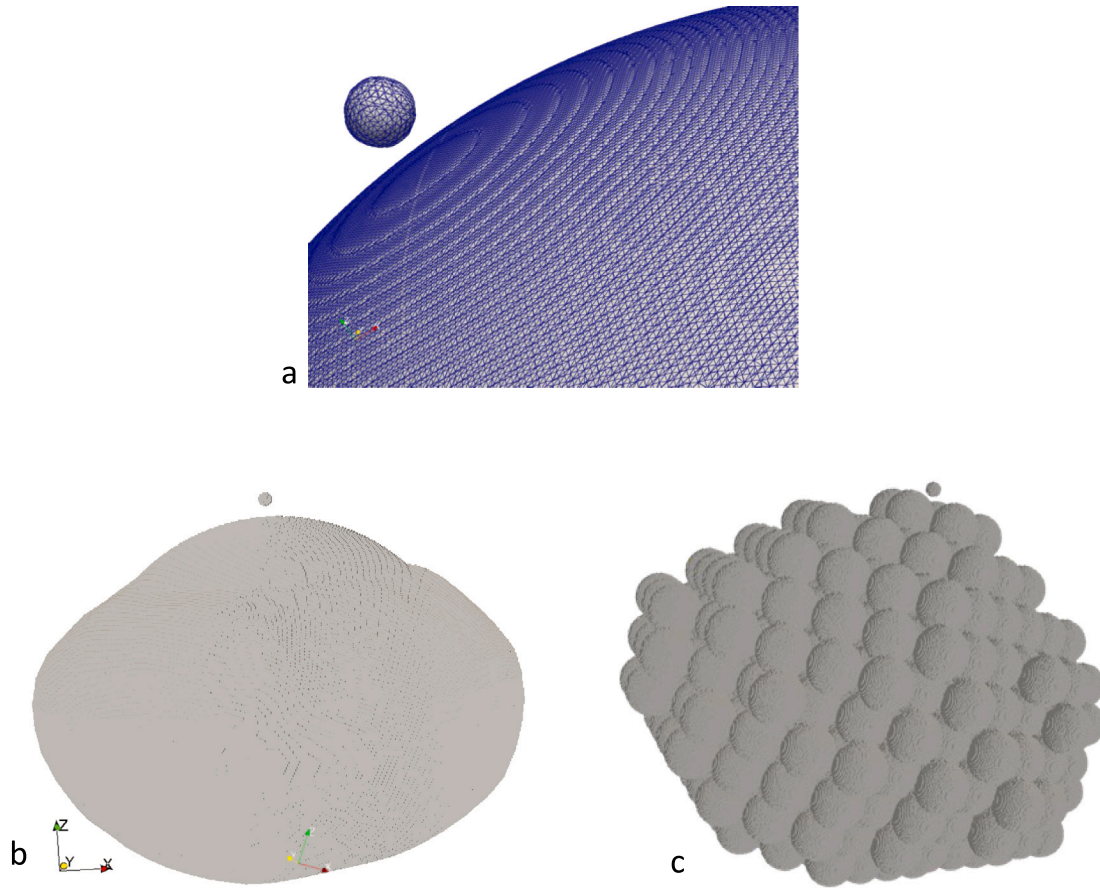
Fig. 3. 3D simulations at initialization, showing setups for uniform pseudo-microporosity and rubble piles. Figure (a) shows a zoomed in region of the 3D mesh with a resolution of 5 cells per projectile radius (cppr), which corresponds to a zone size of 750 m. Figure (b) shows the 3D Cartesian set-up for the case of uniform psuedo-microporosity, and (c) shows the 3D set-up for the hexagonal close packed rubble-pile configuration. Figure (c) is rotated to show the impactor height above the surface, and we note that the spheres are boulders in the rubble-pile and are not SPH.
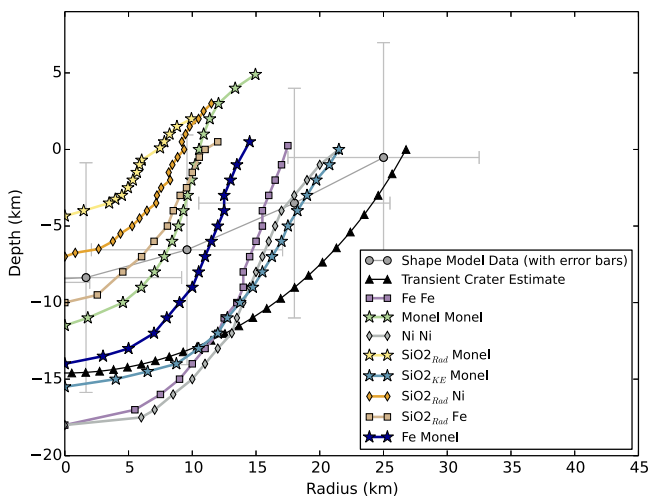

Fig. 4. Crater profiles from 2D axisymmetric simulations using solid materials for both impactor and Psyche. Impactor materials are listed first, followed by materials for Psyche. Profile points from simulations with Monel targets are indicated with stars, those from iron targets are indicated with squares, and those from nickel targets are indicated with diamonds.

Table 2

Results from 2D axisymmetric simulations varying impact velocity for both solid and 50% pseudo-porous targets. Measurements for radius were taken at the pre-impact surface, and measurements for depth were taken at the axisymmetric boundary. For some impacts, underdense material in and above the crater prevented measuring the void material. In these instances, marked with *, a density threshold was applied to remove underdense material before measurements were taken. For impacts into pseudo-porous targets, impact velocities of 6.5 km/s and higher resulted in significant changes in the asteroid. Thus, these craters did not always follow expected morphology because of the effects of the KE, which can lead to asteroid disruption and/or affect the interior of the asteroid.

Impact velocity	Pseudo-Porosity	Crater radius (km)	Crater depth (km)
4 km/s	solid	10.27	10.95
4 km/s	50%	11.50*	15.00*
5.5 km/s	solid	12.25	13.66
5.5 km/s	50%	22.10*	17.4*
6.5 km/s	solid	13.39	15.29
6.5 km/s	50%	–	–
7 km/s	solid	13.85	16.75
7 km/s	50%	37.20	34.25
8.5 km/s	solid	15.28	17.28
8.5 km/s	50%	22.40	9.00
9 km/s	solid	15.67	17.87
9 km/s	50%	18.50	19.50
10 km/s	solid	16.54	18.89
10 km/s	50%	25.50	31.50
12 km/s	solid	17.94	20.50
12 km/s	50%	–	–

increasing pseudo-porosity (or decreasing density) resulted in increased crater dimensions. In particular, less dense targets resulted in deeper craters. Many of the pseudo-microporosity simulations resulted in
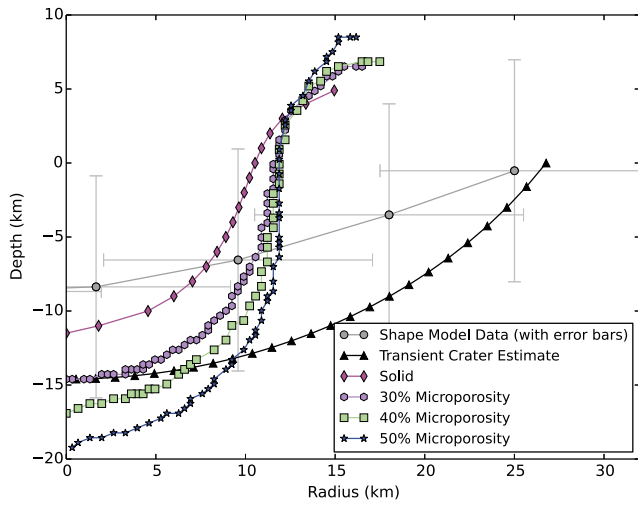
Fig. 5. Crater profiles from 2D axisymmetric simulations modeling Psyche with uniform pseudo-microporosity. The crater profile for the solid simulation is shown for comparison.
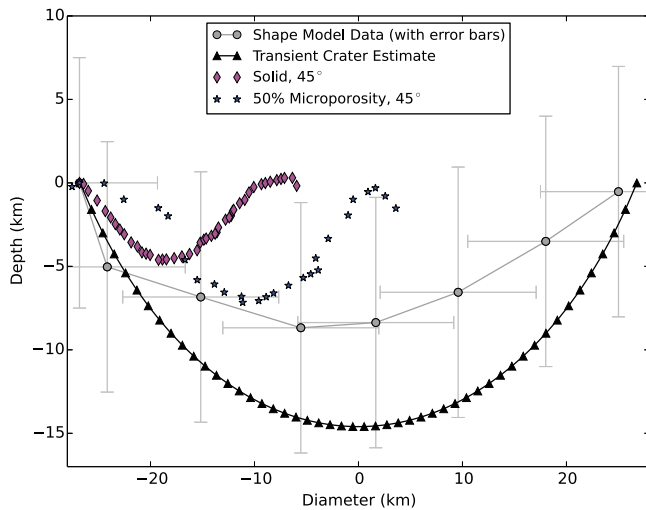

Fig. 6. Crater profiles from 3D Cartesian simulations modeling Psyche with uniform pseudo-microporosity at oblique impact angles 45° from vertical. Simulations with 30% and 40% porosity, as well as simulations at impact angles 60° from vertical, did not run to sufficient times for extracting crater profiles.

depths within or close to the desired range between that of the theoretical transient crater and current shape model data, making these cases good candidates for 3D simulations. We note that because of the 2D simulations being limited to normal impacts, we do not expect crater diameters to match well with this geometry, which also motivates 3D simulations.

In 3D, we tested pseudo-microporosities of 0% (solid), 30%, 40%, and 50% with an impact angle 45° from vertical. In successful simulations, the resulting craters were within the depth uncertainties of the shape model data but failed to match the diameter of the existing crater. Fig. 6 shows the crater profiles from these successful simulations. Because the impacts occurred on a curved surface (the geodesic of the spherical cap), profiles were rotated to allow for direct comparison to theoretical and observed dimensions. The simulation using 50% pseudo-porosity was stopped at a simulation time of about 113.2 s. At this time, no material had a velocity near or above escape velocity, so the crater profile was taken at the end of the simulation without any further modification.

Table 3

Initialization of targets with layered pseudo-microporosity and resulting crater dimensions. Crater radius measurements were taken at the pre-impact surface, and depth measurements are given relative to the pre-impact surface. Bulk densities were calculated using a volume weighted average. Pseudo-porosity is represented by φ, density is represented by ρ, and the initial radius of the core is represented by R_{core}.

Initial target properties					Final crater	
R_{core} (km)	φ_{core} ρ_{core}	h (km)	$\varphi_{surface\_layer}$ $\rho_{surface\_layer}$	φ_{bulk} ρ_{bulk}	radius (km)	depth (km)
100	40% 5.280	25	70% 2.640	54.7% 3.996	12.2	24.5
100	40% 5.280	25	80% 1.760	59.5% 3.566	12.5	28.0
100	50% 4.400	25	60% 3.520	54.9% 3.975	12.1	23.0
100	50% 4.400	25	70% 2.640	59.8% 3.545	12.0	26.5
100	50% 4.400	25	80% 1.760	64.6% 3.115	12.0	30.0
100	60% 3.520	25	70% 2.640	64.9% 3.096	12.1	26.0
100	60% 3.520	25	80% 1.760	69.8% 2.664	12.1	30.5
110	50% 4.400	15	60% 3.520	53.2% 4.124	12.1	21.5
110	50% 4.400	15	70% 2.640	56.4% 3.844	12.1	24.5
110	60% 3.520	15	70% 2.640	63.2% 3.243	12.3	24.5
110	60% 3.520	15	80% 1.760	66.4% 2.963	12.1	24.5
120	60% 3.520	5	70% 2.640	61.2% 3.422	12.9	23.5
120	60% 3.520	5	80% 1.760	62.3% 3.321	13.4	24.5

The crater profiles in Fig. 6 have notably smaller diameters in comparison to the shape model data and transient crater dimensions. In addition, the predicted crater profile for the 50% pseudo-microporosity case appears shallower than the shape model data. Thus, not all aspects of the crater dimensions are well captured, motivating exploration of non-uniform density distributions.

5. Layered pseudo-microporosity results

Moving from a uniform density variations, we now consider layered structures, in which a more dense central core region is surrounded by less dense surface material. Here we address two areas of interest: the effect of varying amounts of pseudo-microporosity and, thus, density variations, within the core and surface regions, and the effect of the thickness of the surface material. We considered compositions that resulted in overall bulk densities within the ranges of current bulk density estimates of Psyche. The overall pseudo-porosities (φ) and bulk densities (ρ) of the configurations tested are shown in Table 3. Bulk densities (ρ) were calculated using a volume weighted average. Fig. 2 shows the initial setup of 3 layered structures considered here, with inner core radii (R_{core}) of 100 km, 110 km, and 120 km, resulting in respective surface layer depths (h) of 25 km, 15 km, and 5 km, for a total target radius of 125 km. The reported crater radius was measured at the pre-impact surface at the end of the simulation, and the crater depth was measured relative near the axisymmetric boundary, also at the end of the simulation, with depth values given relative to the pre-impact surface height.

Fig. 7 shows crater profiles from these simulations. While results from each simulation varied somewhat, the overall trend was the same: the crater depth was affected more than the crater diameter in comparison to the 2D crater profiles shown in Fig. 5 that considered a uniform pseudo-microporosity distribution resulting in constant density throughout Psyche. In general, more dense core regions and less
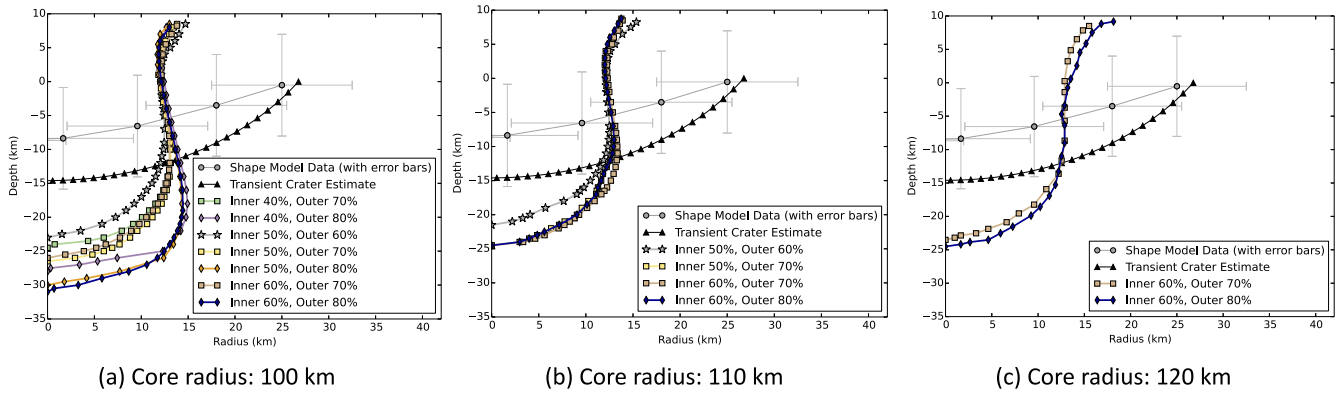
Fig. 7. Crater profiles from 2D axisymmetric simulations modeling Psyche with a more dense core and a less dense outer region, with each region having a different level of pseudo-microporosity. Both Psyche and impactor are modeled as Monel. The pseudo-porosity of the inner, denser core is listed first, followed by the pseudo-porosity of the outer, less dense mantle region. The radius of the inner core is listed for each figure, and Psyche's total radius was 125 km in each simulation.

dense mantle layers resulted in deeper craters. When the mantle layer had extremely low density (80% pseudo-microporosity), the crater shape starts to form a wide, flat base. While the degrees of pseudo-microporosity and materials are different, this corroborates results from Raducan et al. (2020), who also predicted flat-bottomed crater shapes in some layered structures. However, the occurrence of flat-bottomed craters varied from previous results. Raducan et al. found that the presence of flat-bottomed craters was related to the ratio of the outer layer thickness (h) to the crater diameter (D). In our work, the density of the outer layer was the quantity most closely associated with the presence of flat-bottomed craters. We attribute these differences to material differences, and also differences in modeling choices. In our work, the core and mantle layers are the same material (i.e., Monel), varying only in density resulting from pseudo-microporosity, while the materials tested by Raducan et al. included iron and dunite, which have greater variations of material properties. Furthermore, our modeling approach does not include compaction processes, which will have a larger effect on the results for cases in which we tested high pseudo-microporosity materials.

Because these simulations resulted in crater profiles that were far too deep and narrow to reflect the current crater shape, we did not run these compositions in 3D. However, by including the results, we can rule out some material compositions and conclude that Psyche is unlikely to have a layered composition like the ones tested in this work, which employed a single metallic material system with density variations. Simulations involving layered structures with varied materials could still be possible, and further studies would contribute to the overall understanding of Psyche's composition, but such simulations would necessitate using multiple materials and are thus beyond the scope of this single-material study.

6. Rubble-pile configuration results

To consider macroscopic voids, we modeled Psyche as a rubble pile, resulting in an asteroid with varied regions of lower and higher densities. We considered two rubble-pile configurations: regular hexagonal close packing and regular square packing. The hexagonal close packing allows for minimum space between boulders, maximizing the number of boulders with uniform size. The square packing allows for more space between boulders and fewer boulders overall. The boulder radius (12.5 km) was chosen to allow 10 boulders in the vertical direction along a normal impact trajectory. The boulder size was larger than the impactor, but not so large that the effects between a solid target and rubble pile target could not be differentiated. The boulder size was not so small that the computational cost was prohibitively

expensive. We note that the chosen boulder size is an assumed value, and not a physically informed value. In general, the internal structure of a rubble pile is extremely difficult to observe, and thus it must be approximated based on other known properties of an asteroid, which are typically derived from data about the surfaces of asteroids (for more information see Walsh (2018) and references therein). Varying the size of the boulders in the rubble pile, and also investigating the effect of non-uniform boulder structure is left to future work.

The hexagonal packing had a macroporosity of 7.72%. For the case of solid boulders, the bulk density of the total asteroid was 8.130 g/cm^3. For the case in which the boulders had a pseudo-microporosity of 40%, the bulk density was 4.878 g/cm^3. The square packing had macroporosity of 17.4%. The bulk density for solid boulders was 7.280 g/cm^3, while the bulk density for the case of 40% pseudo-microporous boulders was 4.368 g/cm^3. For both packings, the solid cases were consistent with a primarily metallic asteroid and had bulk densities near the higher estimates, while the bulk density of the pseudo-microporosity cases were closer to the median range of bulk density estimates of Psyche.

For our 2D simulations, we chose to use Cartesian coordinates in order to avoid hoop stress effects that would result from an axisymmetric mesh geometry. Fig. 8 shows the 2D rubble-pile configurations for a regular hexagonal close packing (Figs. 8(a)–8(b)) and a regular square packing (Figs. 8(d)–8(e)) during crater excavation and after crater modification. Figs. 8(c) and 8(f) show the pressure wave traveling through each rubble pile about 5 s after impact. In the hexagonal packing, the pressure wave travels in the direction of impact (normal to the pre-impact surface) as well as following trajectories from the sphere's center to the tangent points of other spheres in the packing. For the square packing, the pressure wave travels along the impact trajectory and normal to the impact trajectory, from the sphere's center to the tangents points of other spheres. The different shapes of the pressure waves contribute to the different crater morphologies at the end of the simulations.

Fig. 9 shows the final crater profiles for the 2D rubble-pile simulations, along with the current shape model data and theoretical transient crater. The rubble-pile configurations were the only 2D compositions that resulted in craters as wide as – or wider than – current shape model data. The solid simulations had crater diameters of 77.6 km and 46.5 km for the hexagonal and square packings, respectively. The respective depths were 17.7 km and 22.2 km. For the simulations with pseudo-microporosity, crater diameters were 85.0 km and 54.0 km, respectively, for hexagonal and square packings. The respective depths were 25.0 km and 30.4 km. For comparison, the theoretical transient crater had a diameter of 53.5 km and a depth of 14.6 km.
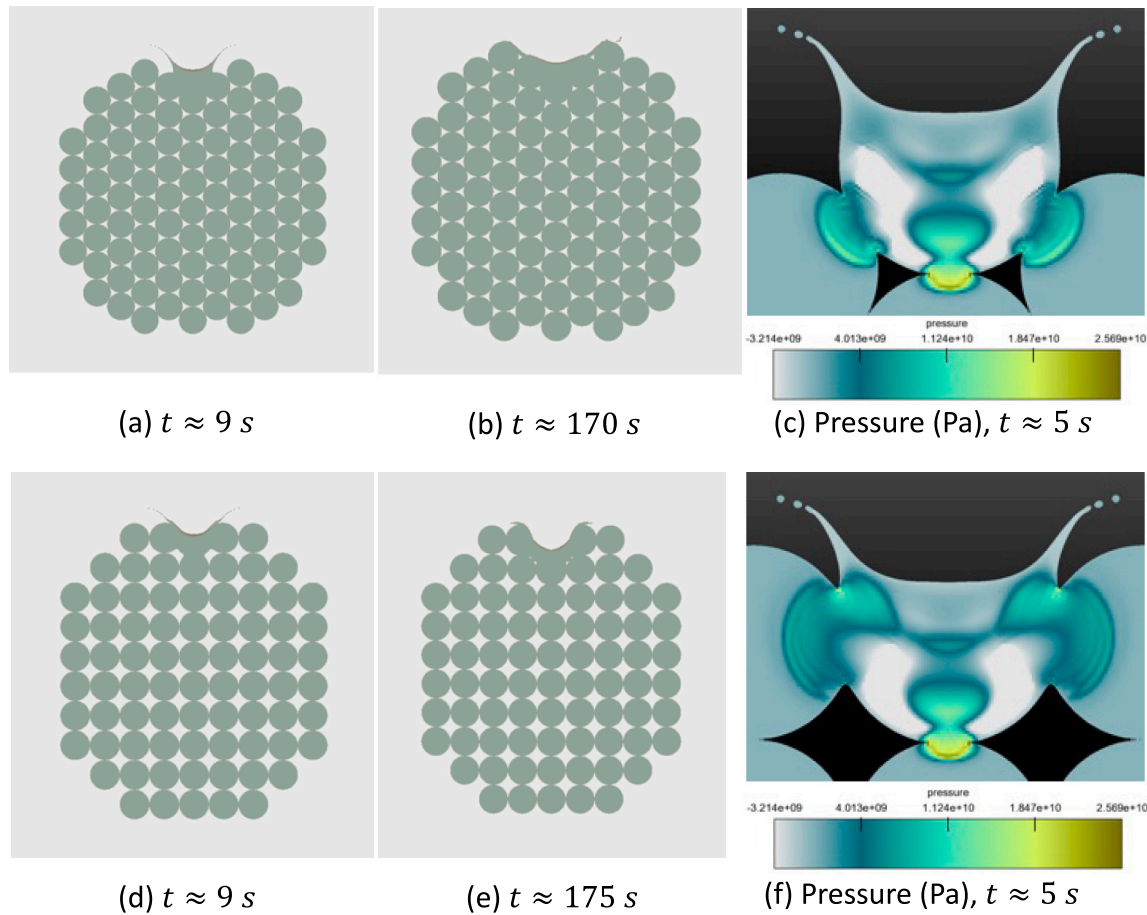
Fig. 8. 2D Cartesian simulations of rubble piles with a regular hexagonal close packing and a regular square packing, (left) during crater excavation, (center) after crater modification, and (right) colored by pressure to show the direction of the shock wave.

We note that while the craters from these simulations are larger than the current crater on Psyche, processes such as impact gardening could have resulted in filling in some of the crater, resulting in a smaller crater today. Further, for the hexagonal packing, the shape of the crater is wide and shallow, consistent with observations of the current crater. Thus, rubble piles should be explored further in 3D to account for their complex structure and to accommodate varied angles of impact, which could demonstrate how varying the location of the impact on a boulder structure affects crater morphology.

Our 3D rubble pile simulations used the hexagonal close packing arrangement for solid boulders and considered impact angles normal to Psyche's surface, 30° from vertical, and 45° from vertical. Considering the 2D simulations, the 2D hexagonal close packing simulations resulted in crater profiles considerably wider than their depths, more consistent with both the theoretical transient crater and current shape model data and thus more likely to yield successful results in 3D.

Fig. 10 shows the final crater profiles from 3D rubble-pile simulations. The angle of impact had a measurable effect on the final crater profile. Each simulation labeled only with the angle of impact began with the impactor positioned above the rubble pile (see Fig. 3(c)), with the impactor traveling along the velocity trajectory toward the rubble pile for about 5 km before impact. Thus, the point at which the impactor first struck a boulder in the rubble pile changed with impact angle. Fig. 2(e) provides a clearer visualization of these effects. An impactor traveling normal to the surface would strike the boulder directly under the impactor, directly above the center of the boulder. An oblique impact would start at the same point but would not strike
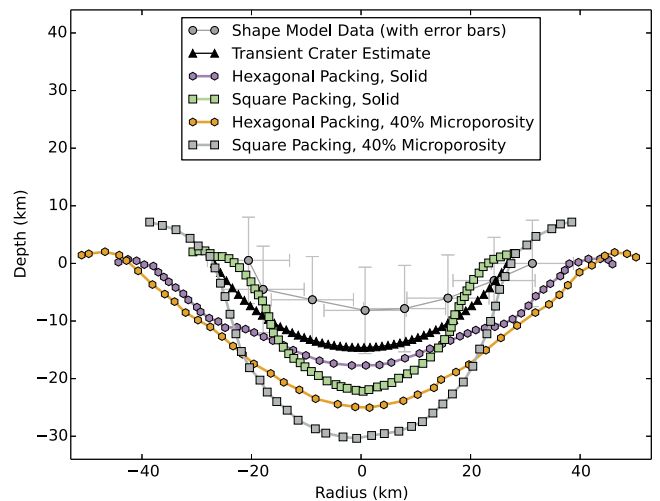

Fig. 9. Crater profiles from 2D Cartesian simulations modeling Psyche as a rubble pile. Both Psyche and impactor are modeled as Monel. Each simulation included macroscopic voids as gaps between the rubble, and some included pseudo-microporosity for the rubble boulders. We modeled Psyche as a regularly packed rubble pile using both hexagonal and square packings. Each rubble pile simulation had a bulk density within the estimated range of Psyche's bulk density.
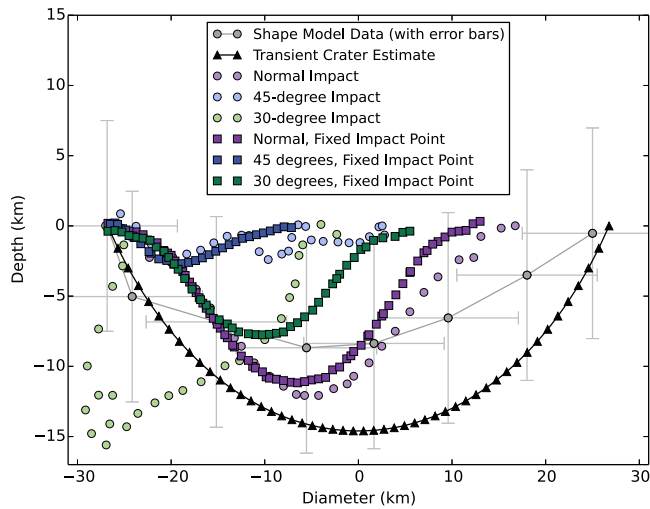
Fig. 10. Crater profiles from 3D Cartesian simulations modeling Psyche as a rubble pile with a regular hexagonal close-packed configuration. For these simulations, we varied the angle of impact, given relative to the normal/vertical position. The pre-impact boulder diameter was about half the crater diameter of the shape model. Because of the pre-impact boulder configuration, the final crater profiles included multiple boulders, which explains the differences in shapes as well as size. The 45-degree impact resulted in a crater that included tangent points for multiple boulders, which is why it appears similar to a complex crater with a central peak, but it is not.

the boulder directly above the center; instead, the impactor would strike a side of the first boulder and continue its trajectory into a region of void material enclosed by other boulders. Thus, the final crater would include the void region and would likely appear larger or deeper than the crater from the normal impact. As a result, these crater profiles vary significantly in shape based on the impact point determined by the velocity vector. These results appear in the figure in pastel colors with circular points along the crater profile. We also considered simulations with a fixed impact point, in which the impactor struck the same location in each simulation, varying only the angle of impact. These results appear in the figure in darker colors with square points along the crater profile. When the impact point is held constant, the oblique impacts resulted in shallower craters, consistent with our previous work in solid and uniformly pseudo-microporous targets (Caldwell et al., 2020).

As in the 3D uniform pseudo-microporosity simulations, crater profiles were rotated to account for the curved impact surface and to allow direct comparison to observed and theoretical results. For impacts into different boulder locations, the normal impact resulted in a crater depth of 12.1 km, between the observed and theoretical profiles. The 30° impact had a depth of 15.6 km, which slightly exceeds the depth of the theoretical transient crater. The 45° impact resulted in a crater that was considerably shallower than the others, with a depth of 2.39 km. Diameter measurements for the oblique impact angles were similar, 24.7 km and 29.3 km, respectively, for the 30° and 45° impacts. These diameters are about half the size of current crater measurements. The normal impact resulted in a crater diameter of 43.5 km, which is within the uncertainties from current measurements when taking into account numerical errors based on mesh resolution (Caldwell et al., 2018). For simulations with a fixed point of impact, the normal impact resulted in a maximum crater depth of 13.7 km, between the observed and theoretical profiles. The 30 ° impact resulted in a maximum crater depth of 9.82 km, which also lies between the theoretical and observed crater depths. In contrast, the 45° impact resulted in a crater with a maximum depth of 4.74 km, shallower than the crater's current observed depth. The crater diameters from the normal, 30°, and 45° impacts were 39.8 km, 32.3 km, and 19.4 km. These measurements were taken in reference to the pre-impact surface at a fixed *y* value of 250 km, which sliced through each crater.

7. Discussion

Overall, a wide range of possible compositions for Psyche, guided by bulk density measurements, were modeled. Matching the crater dimensions proved more difficult in simulations that only considered pseudo-microporosity (i.e., uniform density) compared to our rubble-pile simulations, which considered both pseudo-microporosity and macroscopic voids, i.e., heterogeneous density composition. Table 4 presents bulk density and crater dimensions for the 3D simulations completed here, which include both uniform pseudo-microporosity and rubble-pile configurations. In addition, Fig. 11 shows the ratio between crater depth and diameter for all simulations.

Our simulations strongly suggest that Psyche's internal composition is more likely to include density variations such as those seen in cases with macroscopic voids than to consist solely of uniform density as in simulations considering only pseudo-microporosity. Rubble-pile configurations provided the closest matches to current crater dimensions, and the 3D rubble-pile simulation with a regular hexagonal close packing of solid Monel boulders and a normal impact resulted in depths and diameters well within the uncertainties. Simulations that resulted in dimensions close to – but not within – the uncertainties included impact angles 45° from vertical with rubble piles and uniform pseudo-microporosity. We note that two simulations resulted in depth and diameter within the uncertainties: the 3D regular hexagonal close packings with impacts normal to the surface of Psyche, with the impactor beginning above the surface of Psyche and on the surface of Psyche (referred to as the fixed impact point). We also note that for rubble-pile simulations with a fixed impact point, the depth:diameter ratio decreases as obliquity increases. The 3D simulations in general matched better than their 2D counterparts, and, overall, rubble piles matched better than uniform or layered pseudo-microporosity cases. The 2D simulations of the regular hexagonal close packing resulted in craters that were too wide and too deep, though their depth-to-diameter ratios matched current crater data well. Interestingly, most simulations that produced crater dimensions that compared reasonably to the measured values had bulk densities that were on the higher side of reported bulk densities (see Table 4), which could suggest that Psyche's composition is partially composed of non-metallic components if the bulk density is in fact closer to the mean of measured values. Layered pseudo-microporosity structures with denser cores and lower-density mantles did not match well, despite having bulk density values closer to the mean of the reported measured values (see Table 3).

Our previous work (Caldwell et al., 2020) considered only uniform pseudo-microporosity and Psyche's largest crater. The best match in that case was a 3D simulation of Monel impacting 50% pseudo-porous Monel at an angle 60° from vertical. In comparison, our current results also present similarly close matches for simulations considering uniform pseudo-microporosity and oblique impact angles. In both cases, the resulting crater dimensions were close but not within the range of measured values, and the 60° impact angle tested previously produced results closer than the 45° cases tested here. Thus, these configurations for Psyche's composition cannot be ruled out, particularly if non-metallic components are considered. Of course, our previous work included only uniform densities and did not consider rubble-pile configurations, which were shown in this case to produce even better results in the case of a normal impact. In general, oblique impacts are more likely than normal impacts, though normal impacts cannot be ruled out. Based on the shape of the crater, an oblique impact seemed more likely; however, we were able to achieve the correct shape with normal impacts into a regular hexagonally packed rubble piles rather than oblique impacts into solid or uniformly pseudo-microporous surfaces. Successful rubble-pile simulations with close matches to current crater shapes involved the impactor striking a single boulder along on a trajectory collinear with the tangent points at which boulders are in contact.

Table 4
Table of 3D simulations that either ran to completion or ran long enough that most of the target material movement had ceased at the end of the simulation. Simulations labeled "Rubble, Fixed" indicate rubble-pile simulations for which the point of impact was fixed across all impact angles.

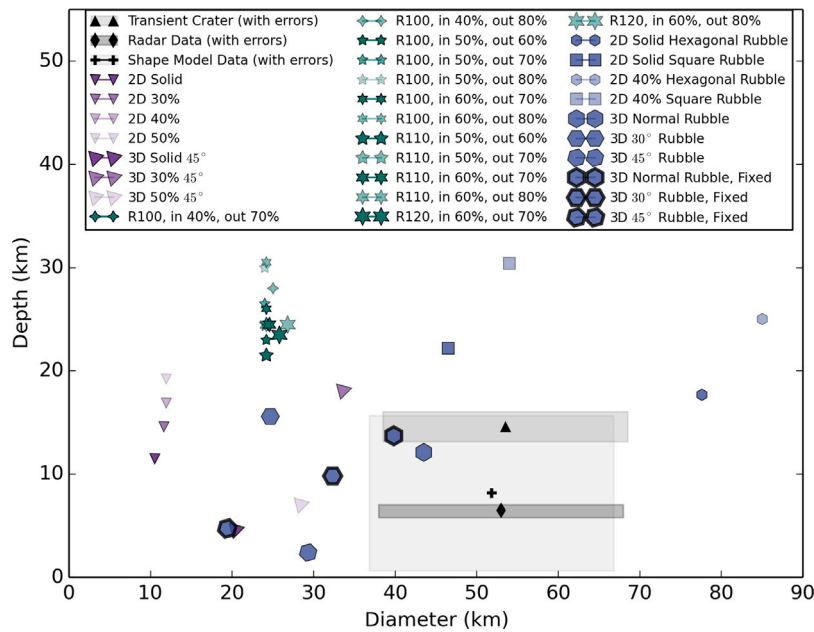| Type	Impact Angle	Bulk Density (g/cm³)	Pseudo-Porosity	Depth (km)	Diameter (km)
Measured	–	3.7–4.1 Lupishko (2006), Viateau (2000), Kochetova (2003), Shepard et al. (2017), Elkins-Tanton et al. (2020), Siltala and Granvik (2021)	–	6.4 ± 0.64 Shepard et al. (2017)	53 ± 15 km Shepard et al. (2017)
Uniform	45°	8.81	0.0%	4.6	20.4
Uniform	45°	6.17	30.0%	18.1	33.6
Uniform	45°	4.41	50.0%	7.07	28.4
Rubble Pile	Normal	6.12	30.0%	12.1	43.5
Rubble Pile	30°	6.12	30.0%	15.6	24.7
Rubble Pile	30°	6.12	30.0%	2.39	29.3
Rubble, Fixed	Normal	6.12	30.0%	13.7	39.8
Rubble, Fixed	30°	6.12	30.0%	9.82	32.3
Rubble, Fixed	45°	6.12	30.0%	4.74	19.4

Fig. 11. Ratios between crater depth and diameter from FLAG simulations.

While the purpose of this study was to focus on density distribution rather than material composition, we can still draw some conclusions regarding the material composition of Psyche from the present work. The general trend of craters being too small indicates that Psyche's material composition is unlikely to be uniformly metallic or uniform in density and is instead likely to contain density variations in the form of rocky components that are more susceptible to deformation than metals. Comparison to recent work by Raducan et al. (2020) also supports this notion. In their simulations of 2D axisymmetric impacts into various possible compositions of Psyche, they found that the wider craters were more likely to have formed from rock materials such as dunite rather than porous metals. However, when simulating impactors similar in size to impactors tested in the current study, they achieved

similar results: smaller crater radii resulting from porous metallic compositions of Psyche, with larger impactors into porous metals resulting in crater dimensions comparable to the crater that is the focus of our current work. Further, as we hypothesize, impacts into rocky asteroids resulted in wider craters than impacts into solid or porous metals.

Finally, our results highlight the need for information beyond bulk density. Our simulations tested a variety of material compositions with similar bulk densities, yet this feature alone was not sufficient for matching crater dimensions. The type of porosity distribution played a larger role than the bulk density itself. Simulations using layered pseudo-porosity had poor matches to current crater dimensions and underperformed both uniform pseudo-microporosity and rubble-pile configurations of Psyche. In addition, the best match came from a
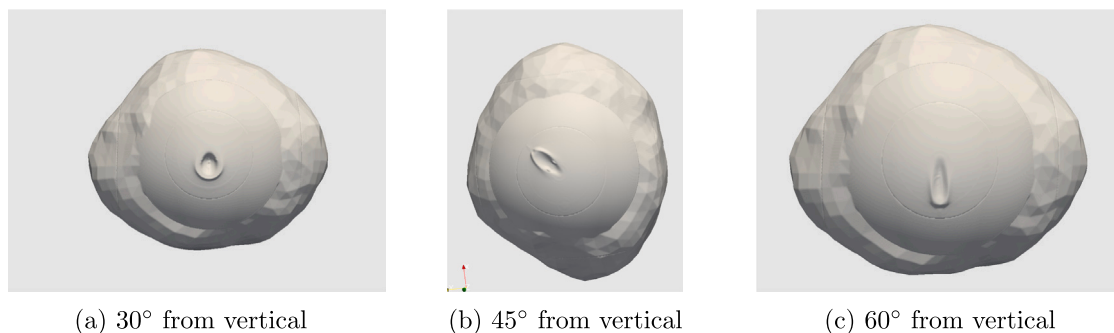
(a) 30° from vertical   (b) 45° from vertical   (c) 60° from vertical

Fig. 12. Final craters from coarse 3D solid simulations of Monel impacting Monel at varied impact angles. The crater rim shape appears to correlate with the angle of impact, with steeper impacts resulting in circular rims and shallower impacts resulting in elliptical rims.

Psyche model with a bulk density on the high end of Psyche's estimated range. In fact, this rubble-pile configuration only considered macroscopic voids (i.e., boulders were modeled as solid), so the amount of pseudo-microporosity within boulders maybe very low. Thus, it is likely that, if Psyche is indeed a rubble pile, some portion of its material composition includes non-metallic components with lower densities, such as carbon and silicates.

8. Conclusions

Our simulations indicate that Psyche is more likely to be a rubble pile of multiple solid boulders than a single body with either uniform or layered density variations. Simulations modeling Psyche as a uniform rubble pile resulted in crater profiles with depth-to-diameter ratios more closely resembling Psyche's deepest impact crater than simulations with other pseudo-porosity configurations. Furthermore, the 3D simulation with a regular hexagonal packing of solid boulders and a normal impact angle resulted in a crater with depth and diameter values within the uncertainties.

We cannot rule out microporous compositions with an oblique impact angle from our simulations alone, although such a composition is less likely to be found in a large asteroid such as Psyche. Our results demonstrate that bulk density alone is insufficient when modeling target asteroids in impact cratering simulations. Our simulations considered a variety of pseudo-porosity distributions and compositions with similar bulk densities using a single material, and the resulting craters varied considerably in these simulations. Forthcoming discovery missions, including the planned mission to Psyche, can benefit from our results by focusing on gathering data not only on bulk densities but also on microporosity, macroporosity, and near-surface porosity.

Declaration of competing interest

The authors have no competing interests to disclose.

Data availability

The authors are unable or have chosen not to specify which data has been used.

Appendix A. 3D solid results

Figs. 12(a)–12(c) show preliminary results from 3D solid simulations of Monel impactors and targets varying the angle of impact. These solid profiles were excluded from the main text because of the coarse resolution, which does not guarantee convergence. However, these images do provide a reference for crater dimensions related to the angle of impact. The steeper impact angles (closer to normal) resulted in crater rims that were closer to circular, while impact angles with greater variation from vertical resulted in more elliptical crater rims.

Appendix B. Parameter sets

See Tables 5–8.

Table 5
Mie-Grüneisen equation of state parameters for Monel (Steinberg, 1996).

FLAG parameter	Parameter definition	Value	Units
r0	Density	8810.	kg/m³
c	Bulk sound speed	4190.	m/s
b	γ volume dependence coefficient	0.49	–
g0	Grüneisen γ	1.95	–
s1	Hugoniot slope coefficient	1.54	–
eta_max	Maximum compression	2.75	–

Table 6
Steinberg–Guinan material model parameters for Monel (Steinberg, 1996).

FLAG parameter	Parameter definition	Value	Units
r0	Density	8810.	kg/m³
sm0	Initial shear modulus	6.88e10	Pa
y0	Initial yield strength	8.3e8	Pa
xn	Work-hardening parameter	0.23	–
yb	Work-hardening parameter	36.	–
yx	Work-hardening maximum	1.92e9	Pa

Table 7
Steinberg–Guinan shear modulus model parameters for Monel (Steinberg, 1996).

FLAG parameter	Parameter definition	Value	Units
r0	Density	8810.	kg/m³
sm0	Initial shear modulus	6.88e10	Pa
au	Shear modulus pressure dependence	2.47e−11	Pa⁻¹
bu	Shear modulus temperature dependence	1.45e−4	K⁻¹

Table 8
Internally calculated Steinberg–Guinan material model parameters for Pseudo-Porous Monel (Steinberg, 1996).

Pseudo-Porosity	FLAG parameter	Parameter definition	Initial value	Units
30%	r0	Density	6167	kg/m^3
	sm0	Initial shear modulus	4.82e10	Pa
	y0	Initial yield strength	5.8e8	Pa
40%	r0	Density	5286	kg/m^3
	sm0	Initial shear modulus	4.13e10	Pa
	y0	Initial yield strength	5.0e8	Pa
50%	r0	Density	4405	kg/m^3
	sm0	Initial shear modulus	3.44e10	Pa
	y0	Initial yield strength	4.2e8	Pa
60%	r0	Density	3524	kg/m^3
	sm0	Initial shear modulus	2.75e10	Pa
	y0	Initial yield strength	3.3e8	Pa
70%	r0	Density	2643	kg/m^3
	sm0	Initial shear modulus	2.06e10	Pa
	y0	Initial yield strength	2.5e8	Pa
80%	r0	Density	1762	kg/m^3
	sm0	Initial shear modulus	1.38e10	Pa
	y0	Initial yield strength	1.7e8	Pa

References

Burchell, M., Mackay, N., 1998. Crater ellipticity in hypervelocity impacts on metals. J. Geophys. Res. 103, 22,761–22,774.

Burchell, M.J., Whitehorn, L., 2003. Oblique incidence hypervelocity impacts on rock. Mon. Not. R. Astron. Soc. 341 (1), 192–198.

Burton, D., 1992. Connectivity Structures and Differencing Techniques for Staggered-Grid Free-Lagrange Hydroynamics. UCRL-JC-110555, Lawrence Livermore National Laboratory, Livermore, C.A..

Burton, D., 1994a. Consistent Finite-Volume Discretization of Hydrodynamic Conservation Laws for Unstructured Grids. UCRL-JC-118788, Lawrence Livermore National Laboratory, Livermore, C.A..

Burton, D., 1994b. Multidimensional Discretization of Conservation Laws for Unstructured Polyhedral Grids. UCRL-JC-118306, Lawrence Livermore National Laboratory, Livermore, C.A..

Caldwell, W.K., 2019. Differential Equation Models for Understanding Phenomena beyond Experimental Capabilities. Arizona State University.

Caldwell, W., Euser, B., Plesko, C., Larmat, C., Lei, Z., Knight, E., Rougier, E., Hunter, A., 2021. Benchmarking numerical methods for impact and cratering applications. Appl. Sci. 11 (6), 2504.

Caldwell, W.K., Hunter, A., Plesko, C.S., Wirkus, S., 2018. Verification and validation of the FLAG Hydrocode for impact cratering simulations. J. Verif. Valid. Uncertain. Quantif. 3 (3), 031004.

Caldwell, W.K., Hunter, A., Plesko, C.S., Wirkus, S., 2020. Understanding Asteroid 16 Psyche's composition through 3D impact crater modeling. Icarus 351, 113962.

Carry, B., 2012. Density of asteroids. Planet. Space Sci. 73, 98–118.

Davison, T., Collins, G., Elbeshausen, D., Wunnemann, K., Kearsley, A., 2011. Numerical modeling of oblique hypervelocity impacts on strong ductile targets. Meteorit. Planet. Sci. 46, 1510–1524.

Elbeshausen, D., Wunnemann, K., 2013. The transition from circular to elliptical impact craters. J. Geophys. Res. Plan. 118, 2295–2309.

Elkins-Tanton, L., Asphaug, E., Bell III, J., Bercovici, H., Bills, B., Binzel, R., Bottke, W., Dibb, S., Lawrence, D., Marchi, S., et al., 2020. Observations, meteorites, and models: A preflight assessment of the composition and formation of (16) psyche. J. Geophys. Res. Plan. 125 (3), e2019JE006296.

Farinella, P., Davis, D.R., 1992. Collision rates and impact velocities in the main asteroid belt. Icarus 97 (1), 111–123.

Flynn, G., Moore, L., Klöck, W., 1999. Density and porosity of stone meteorites: Implications for the density, porosity, cratering, and collisional disruption of asteroids. Icarus 142, 97–105.

French, B.M., 1998. Traces of Catastrophe: A Handbook of Shock-Metamorphic Effects in Terrestrial Meteorite Impact Structures. Technical report.

Gault, D.E., Wedekind, J.A., 1978. Experimental studies of oblique impact. In: Lunar and Planetary Science Conference Proceedings. Vol. 9. pp. 3843–3875.

Grieve, R.A., 1991. Terrestrial impact: The record in the rocks. Meteoritics 26 (3), 175–194.

Grieve, R.A., Cintala, M.J., 1982. A method for estimating the initial impact conditions of terrestrial cratering events, exemplified by its application to Brent crater, Ontario. In: Lunar and Planetary Science Conference Proceedings. Vol. 12. pp. 1607–1621.

Harrison, W., Loupias, C., Outrebon, P., Turland, D., 1995. Experimental data and hydrocode calculations for hypervelocity impacts of stainless steel into aluminium in the 2–8 km/s range. Int. J. Impact Eng. 17 (1–3), 363–374.

Hill, J.L., 2017. User's Manual for FLAG Version 3.6.0. The Lagrangian Applications Project, Los Alamos National Laboratory, LA-CP-17-20057.

Holsapple, K.A., 1993. The scaling of impact processes in planetary sciences. Ann. Rev. Earth Plan. Sci. 21 (1), 333–373.

Housen, K., Holsapple, K., 2003. Impact cratering on porous asteroids. Icarus 163, 102–119.

Housen, K., Holsapple, K., Voss, M., 1999. Compaction as the origin of the unusual craters on the asteroid Mathilde. Nature 402, 155–157.

Kenamond, M., 2020. (U) AMR in FLAG. LA-UR-20-27533, Los Alamos National Laboratory, Los Alamos, N.M..

Kochetova, O., 2003. Application of new criteria for the selection of perturbed minor planets to the determination of the masses of perturbing minor planets by the dynamical method. Soobshch. in-ta Prikladnoi Astronomii RAN (165), 42.

Krygier, A., Powell, P., McNaney, J., Huntington, C., Prisbrey, S., Remington, B., Rudd, R., Swift, D., Wehrenberg, C., Arsenlis, A., et al., 2019. Extreme hardening of Pb at high pressure and strain rate. Phys. Rev. Lett. 123 (20), 205701.

Kumamoto, K.M., Owen, J.M., Syal, M.B., Pearl, J., Raskin, C., Caldwell, W.K., Rainey, E., Stickle, A.M., Daly, R.T., Barnouin, O., 2022. Predicting asteroid material properties from a DART-like kinetic impact. Plan. Sci. J. 3 (10), 237.

Lupishko, D., 2006. On the bulk density of the M-type asteroid 16 psyche. Solar Syst. Res. 40 (3), 214–218.

Melosh, H.J., 1989. Impact Cratering: A Geologic Process. Oxford University Press, Clarendon Press, New York, Oxford.

Melosh, H.J., 2011. Planetary Surface Processes. Vol. 13. Cambridge University Press.

Nishida, M., Hayashi, K., Toya, K., 2019. Influence of impact angle on size distribution of fragments in hypervelocity impacts. Int. J. Impact Eng. 128, 86–93.

Ogawa, R., Nakamura, A.M., Suzuki, A.I., Hasegawa, S., 2021. Crater shape as a possible record of the impact environment of metallic bodies: Effects of temperature, impact velocity and impactor density. Icarus 362, 114410.

Oh, D.Y., Goebel, D.M., Elkins-Tanton, L., Polanskey, C., Lord, P., Tilley, S., Snyder, J.S., Carr, G., Collins, S., Lantoine, G., et al., 2016. Psyche: Journey to a metal world. In: 52nd AIAA/SAE/ASEE Joint Propulsion Conference. p. 4541.

Peng, J., Hu, C., Li, Y., Zhang, L., Jing, F., 2008. Determination of parameters of Steinberg-Guinan constitutive model with shock wave experiments. Internat. J. Modern Phys. B 22 (09n11), 1111–1116.

Pierazzo, E., Artemieva, N., Asphaug, E., Baldwin, E., Cazamias, J., Coker, R., Collins, G., Crawford, D., Davison, T., Elbeshausen, D., et al., 2008. Validation of numerical codes for impact and explosion cratering: Impacts on strengthless and metal targets. Meteorit. Planet. Sci. 43 (12), 1917–1938.

Plesko, C., Biwer, C., Boslough, M., Caldwell, W., Harwell, M., Margolin, L., 2019. Impact hazard mitigation of a highly porous contact binary asteroid. Phys. Rev. E 90, 033107.

Raducan, S., Davison, T., Collins, G., 2020. Morphological diversity of impact craters on asteroid (16) Psyche: Insight from numerical models. J. Geophys. Res. Plan. 125 (9), 1–19.

Riller, U., 2005. Structural characteristics of the Sudbury impact structure, Canada: Impact-induced versus orogenic deformation – A review. Meteorit. Planet. Sci. 40 (11), 1723–1740.

Shepard, M.K., Richardson, J., Taylor, P.A., Rodriguez-Ford, L.A., Conrad, A., de Pater, I., Adamkovics, M., de Kleer, K., Males, J.R., Morzinski, K.M., et al., 2017. Radar observations and shape model of asteroid 16 Psyche. Icarus 281, 388–403.

Shoemaker, L.E., Smith, G.D., 2006. A century of monel metal: 1906–2006. JOM 58 (9), 22–26.

Siltala, L., Granvik, M., 2021. Mass and density of asteroid (16) Psyche. Astrophys. J. Lett. 909 (L14), 1–5.

Steinberg, D., 1996. Equation of State and Strength Properties of Selected Materials. UCRL-MA-106439, Lawrence Livermore National Laboratory, Livermore, C.A..

Steinberg, D., Cochran, S., Guinan, M., 1980. A constitutive model for metals applicable at high-strain rate. J. Appl. Phys. 51 (3), 1498–1504.

Stickle, A.M., DeCoster, M.E., Burger, C., Caldwell, W.K., Graninger, D., Kumamoto, K.M., Luther, R., Ormö, J., Raducan, S., Rainey, E., et al., 2022. Effects of impact and target parameters on the results of a kinetic impactor: Predictions for the Double Asteroid Redirection Test (DART) mission. Plan. Sci. J. 3 (11), 248.

Stickle, A.M., Syal, M.B., Cheng, A.F., Collins, G.S., Davison, T.M., Gisler, G., Güldemeister, N., Heberling, T., Luther, R., Michel, P., et al., 2020. Benchmarking impact hydrocodes in the strength regime: Implications for modeling deflection by a kinetic impactor. Icarus 338, 113446.

Suzuki, A.I., Fujita, Y., Harada, S., Kiuchi, M., Koumoto, Y., Matsumoto, E., Omura, T., Shigaki, S., Taguchi, E., Tsujido, S., et al., 2021. Experimental study concerning the oblique impact of low-and high-density projectiles on sedimentary rocks. Planet. Space Sci. 195, 105141.

Viateau, B., 2000. Mass and density of asteroids (16) Psyche and (121) Hermione. Astron. Astrophys. 354, 725–731.

Vogler, T., Ao, T., Asay, J.R., 2009. High-pressure strength of aluminum under quasi-isentropic loading. Int. J. Plast. 25 (4), 671–694.

Walsh, K.J., 2018. Rubble pile asteroids. Annu. Rev. Astron. Astrophys. 56, 593–624.